



Cite this: *Energy Environ. Sci.*, 2016, 9, 3531

High current density, long duration cycling of soluble organic active species for non-aqueous redox flow batteries†

Jarrold D. Milshtein,^{‡,ab} Aman Preet Kaur,^{‡,c} Matthew D. Casselman,^c Jeffrey A. Kowalski,^{ad} Subrahmanyam Modekrutti,^c Peter L. Zhang,^c N. Harsha Attanayake,^c Corrine F. Elliott,^c Sean R. Parkin,^c Chad Risko,^{ce} Fikile R. Brushett^{*ad} and Susan A. Odom^{*c}

Non-aqueous redox flow batteries (NAqRFBs) employing redox-active organic molecules show promise to meet requirements for grid energy storage. Here, we combine the rational design of organic molecules with flow cell engineering to boost NAqRFB performance. We synthesize two highly soluble phenothiazine derivatives, *N*-(2-methoxyethyl)phenothiazine (MEPT) and *N*-[2-(2-methoxyethoxy)ethyl]phenothiazine (MEEPT), via a one-step synthesis from inexpensive precursors. Synthesis and isolation of the radical-cation salts permit UV-vis decay studies that illustrate the high stability of these open-shell species. Cyclic voltammetry and bulk electrolysis experiments reveal the promising electrochemical properties of MEPT and MEEPT under dilute conditions. A high performance non-aqueous flow cell, employing interdigitated flow fields and carbon paper electrodes, is engineered and demonstrated; polarization and impedance studies quantify the cell's low area-specific resistance (3.2–3.3 Ω cm²). We combine the most soluble derivative, MEEPT, and its tetrafluoroborate radical-cation salt in the flow cell for symmetric cycling, evincing a current density of 100 mA cm⁻² with undetectable capacity fade over 100 cycles. This coincident high current density and capacity retention is unprecedented in NAqRFB literature.

Received 14th July 2016,
Accepted 15th September 2016

DOI: 10.1039/c6ee02027e

www.rsc.org/ees

Broader context

The intermittent nature of renewable energy technologies, a growing fraction of the electric power sector, and the need for improved electrical grid efficiency are driving the development of grid-scale energy storage devices. Redox flow batteries are an especially attractive technology for these applications due to scalability, ease of manufacturing, and long lifetimes, but are currently too expensive for grid deployment. Typically, aqueous flow batteries have been at the forefront of device development, but non-aqueous flow batteries could offer several advantages including higher voltage, higher energy density, and lower materials costs. Despite this technical potential and a recent flurry of research activity in the field, non-aqueous flow batteries have yet to demonstrate the stability or performance to compete with the more well developed aqueous systems. As such, this work entails the design of stable, energy-storing organic molecules with facile syntheses from cheap precursors, which could lead to low-cost materials and improved cell performance. In addition, we engineer a high performance battery architecture to evaluate these new materials at economically relevant rates, bringing non-aqueous flow battery devices to a technology-readiness level that might soon compete with their aqueous counterparts. The multi-scale molecular and cell-level engineering principles outlined can apply to other flow-battery chemistries to boost performance.

^a Joint Center for Energy Storage Research, USA

^b Department of Materials Science and Engineering, Massachusetts Institute of Technology, Cambridge, MA 02139, USA

^c Department of Chemistry, University of Kentucky, Lexington, KY 40506, USA. E-mail: susan.odom@uky.edu

^d Department of Chemical Engineering, Massachusetts Institute of Technology, Cambridge, MA 02139, USA. E-mail: brushett@mit.edu

^e Center for Applied Energy Research, University of Kentucky, Lexington, KY 40511, USA

† Electronic supplementary information (ESI) available: NMR spectra, cyclic voltammetry, bulk electrolysis, flow cell experiments. CCDC 1451232 and 1492208–1492210. For ESI and crystallographic data in CIF or other electronic format see DOI: 10.1039/c6ee02027e

‡ The authors contributed equally to the manuscript.

Introduction

Grid energy storage has emerged as a critical technology for improving the sustainability of electricity generation by alleviating the intermittency of renewables (*i.e.*, solar, wind), improving the efficiency of the existing fossil fuel infrastructure via load levelling and arbitrage, and providing high value services such as back-up power, frequency regulation, and voltage support.^{1,2} Redox flow batteries (RFBs) are rechargeable electrochemical devices that store energy in soluble active species dissolved in liquid-phase electrolytes; the electrolytes

are housed in external tanks and pumped through a power-converting reactor.^{3–8} These secondary batteries boast long lifetimes, ease of manufacturing, and independence between scaling power (reactor size) and energy (tank volume), thereby offering a feasible route to low-cost grid storage.^{3–8} Despite these promising attributes, existing RFB chemistries are currently too expensive for broad adoption.⁹ Although the majority of RFBs are based on aqueous chemistries,^{3,7} transitioning from aqueous to non-aqueous systems provides the opportunity to increase cell potentials *via* wider electrolyte-stability windows.^{6,7,10–13} Further, new electrochemical couples that are incompatible with aqueous electrolytes due to low solubility, chemical reactivity, or redox potentials outside the electrolyte-stability window may become viable under non-aqueous conditions. In combination, these augmentations could improve energy density and subsequently enable low-cost energy storage, if the appropriate active and inactive materials are identified.⁹

Several classes of redox-active materials have been investigated for non-aqueous (NAq) RFBs, including organic molecules,^{14–25} metal-centered complexes,^{26–38} and redox-active macro-architectures.^{39–41} Redox-active organic molecules are of particular interest for RFBs because key electrochemical and physical properties can be tailored using the principles of molecular engineering.¹² Moreover, organic molecules are comprised of earth-abundant elements (*e.g.*, hydrogen, carbon, nitrogen, oxygen, sulfur); materials reserves and production rates do not determine the price of materials, thereby reducing manufacturing costs. Although organic NAqRFBs may enable cost-effective grid storage,⁹ the field is relatively young, and economically feasible system performance has yet to be realized. To date, reports have focused on molecular discovery and electrochemical characterization under dilute conditions,^{19,23,24} with only a few attempts to engineer performance systems with highly soluble active species^{18,20,22,24} or advanced flow-cell designs.^{30,42} Simultaneous engineering at the molecular and cell levels is a challenging task because NAqRFB failure might arise from active species degradation (*e.g.*, charged species decay) or from inadequate flow cell design (*e.g.*, high resistance, membrane fouling, crossover). Advancing the field will require demonstrating cycling of an organic molecule with a long lifetime at a high current density.

Many classes of redox-active organic molecules have been proposed for use in NAqRFBs, such as anthraquinones⁴³ and dialkoxybenzenes.^{16,17,23,24} Of the proposed redox-active organic molecules, nearly all, with the exception of *N*-oxidanyl amines (*e.g.*, TEMPO),^{14,22,25} suffer from rapid capacity fade or poor solubility.^{17,38} *N*-Ethylphenothiazine (EPT, Fig. 1a) is a commercially available and stable electron-donating organic molecule that oxidizes at ~ 0.3 V *vs.* ferrocene/ferrocenium (Fc/Fc⁺) in carbonate electrolytes. The long lifetime of this molecule as an overcharge protection material in lithium-ion batteries highlights its remarkable stability.^{44–47} Our studies have further demonstrated the stability of EPT in aprotic, organic solvents, both in the neutral and singly oxidized (radical-cation) states.⁴⁸ This stability suggests that EPT could serve as a one-electron-donating material in NAqRFB electrolytes, but the solubility of EPT in carbonate- or nitrile-based solvents (~ 0.1 M) is too low

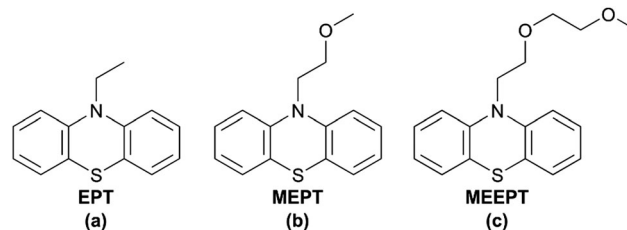


Fig. 1 Chemical structures of (a) *N*-ethylphenothiazine (EPT), (b) *N*-(2-methoxyethyl)phenothiazine (MEPT), and (c) *N*-(2-(2-methoxyethoxy)ethyl)phenothiazine (MEEPT).

for practical implementation.⁹ By comparison, we reported previously that 3,7-bis(trifluoromethyl)-*N*-ethylphenothiazine (BCF3EPT),^{18,47} an EPT derivative, dissolves at concentrations up to 2 M in non-aqueous electrolytes and is even more stable than EPT.⁴⁷ The synthesis of BCF3EPT, however, requires multiple steps, the last of which entails a low-yielding trifluoromethylation reaction.⁴⁷ Ideally, organic active materials for NAqRFBs will be easily synthesized from cheap precursors, leading to active-material costs $\leq \$5$ kg⁻¹. Additionally, active materials should be highly soluble (>1 M) to ensure that electrolytes are sufficiently energy-dense and low-cost to be economically viable.⁹

Furthermore, NAqRFB design has failed to incorporate advanced flow-cell architectures developed for aqueous RFBs over the past few years.^{49,50} Organic-based aqueous RFBs have demonstrated vast reductions in area-specific resistance (ASR) by transitioning from initial prototypes⁵¹ to advanced cell designs^{52,53} inspired by all-vanadium RFB literature. Many NAqRFBs implement thick (>1 mm) flow through electrodes, leading to large ohmic and mass-transfer resistances, subsequently forcing cell operation at low current densities only.^{31,35} Prior work on vanadium RFBs suggests that zero-gap,^{49,50} interdigitated flow fields (IDFFs) with thin (<500 μ m) carbon-paper electrodes will offer the best balance of ASR and pressure drop for at-scale RFBs.^{54,55} The IDFF requires that all electrolyte flows through a short path of porous electrode, enabling high current densities, but not developing an unacceptably large pressure drop.^{54,55} Thin carbon-paper electrodes offer a balance of high surface area, good mass transport, and low ohmic resistance.⁵⁰ We previously reported a flow cell with IDFFs and carbon-paper electrodes designed for compatibility with non-aqueous electrolytes,⁴² but no demonstration of cycling of an organic active species in such a flow cell has been reported.

In this work, we engage in molecular and cell-level engineering to afford high-rate, long-duration cycling of soluble EPT derivatives. We first describe the synthesis and solubility of two new phenothiazine derivatives, *N*-(2-methoxyethyl)phenothiazine (MEPT, Fig. 1b) and *N*-[2-(2-methoxyethoxy)ethyl]phenothiazine (MEEPT, Fig. 1c), as well as the stability of their tetrafluoroborate radical-cation salts. These compounds are synthesized in a single step from an inexpensive, commercially available precursor. Both neutral species have significantly lower melting points and higher solubilities in non-aqueous electrolytes than EPT. MEEPT, in fact, is a liquid at room temperature. We investigate the fundamental

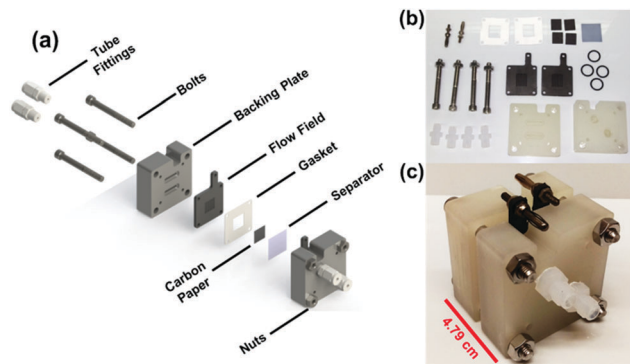


Fig. 2 (a) Schematic of the non-aqueous-compatible flow cell employed in this work, exhibiting IDFFs and carbon paper electrodes. (b) Photograph of the flow cell components. (c) Photograph of the assembled flow cell.

electrochemical properties of these new phenothiazine derivatives using cyclic voltammetry (CV) to determine redox potentials, chemical reversibility, and diffusion coefficients, and use bulk electrolysis to examine cycling behavior under dilute conditions. Next, we employ the most soluble derivative (MEEPT) at a moderate concentration (0.5 M active species) in a high-performance flow cell (Fig. 2) incorporating IDFFs and carbon-paper electrodes. This flow cell exhibits the lowest reported cell ASR for NAqRFBs ($3.2\text{--}3.3\ \Omega\ \text{cm}^2$), allowing the stable MEEPT molecule to cycle at an aggressive current density of $100\ \text{mA}\ \text{cm}^{-2}$ with negligible capacity fade over 100 cycles. The molecular and cell engineering principles outlined in this paper, aimed at high concentration, high stability, and high current densities, apply to other emerging redox chemistries and provide a framework for advancing NAqRFBs towards a technology-readiness level competitive with aqueous RFBs.

Results and discussion

Synthesis and stability

Deprotonation of phenothiazine and a subsequent $\text{S}_{\text{N}}2$ reaction with the corresponding alkyl halide produces EPT, MEPT, or MEEPT in good yields (Fig. 3). MEPT is a white, crystalline solid with a melting point ($47\ ^\circ\text{C}$) significantly lower than that of EPT ($103\text{--}104\ ^\circ\text{C}$). MEEPT is a pale yellow liquid at room temperature. NMR (Fig. S1–S4, ESI[†]), mass spectrometry, and elemental analysis confirm product structure and purity.

While phenothiazines have been extensively studied for applications in lithium-ion battery overcharge protection,^{44–46,48} the design constraints for RFB active materials are fundamentally

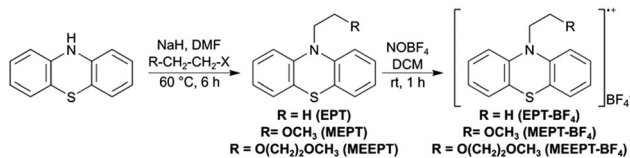


Fig. 3 Synthesis of EPT, MEPT, and MEEPT via the alkylation of phenothiazine and subsequent preparation of the radical-cation salts via chemical oxidation.

different than those for overcharge protection. Redox-active materials for RFBs must achieve higher concentrations and have a lower cost per unit mass. We have previously investigated a highly soluble phenothiazine derivative for RFB applications,⁴⁷ but the low yielding, multi-step synthesis currently renders the material infeasible for low-cost NAqRFBs. Hence, the simple one step synthesis from cheap precursors outlined in Fig. 3 represents a new approach towards achieving a low-cost, soluble active species for NAqRFBs.

Isolation of a neutral redox-active molecule does not ensure the stability of the radical-cation form, which is typically the more reactive state of a redox-active organic couple. To enable stability studies of the radical cation itself, we synthesized tetrafluoroborate radical-cation salts via chemical oxidation of the neutral molecules with nitronium tetrafluoroborate (NOBF_4) (Fig. 3). We employed single crystal XRD to identify the structures of the radical-cation salts and confirm their chemical compositions (Fig. 4), and EPR (Fig. S5, ESI[†]) of solutions containing these salts in dichloromethane (DCM) to confirm the presence of a radical species. The EPR spectra are consistent with our previous reports of the hexachloroantimonate radical-cation salt of EPT,⁴⁸ an expected result due to the similar electronic structure of these *N*-alkylated phenothiazine species.

UV-vis absorption spectroscopy can monitor the lifetimes of radical cations that absorb visible light; this technique has been used to evaluate redox shuttle candidates for overcharge protection of lithium-ion batteries.^{45,46} Herein, we employed UV-vis to compare the stability of dilute solutions of EPT- BF_4 , MEPT- BF_4 , or MEEPT- BF_4 radical-cation salts in acetonitrile (ACN) and propylene carbonate (PC). Fig. 5 depicts the absorption spectra of the three radical-cation salts at 0, 1, 3, 5, and 24 h after dissolution in ACN. We also performed the same analysis using PC as the solvent (Fig. S7, ESI[†]). The spectra are nearly identical for EPT- BF_4 , MEPT- BF_4 , and MEEPT- BF_4 , exhibiting characteristic peaks at the following wavelengths: 316, 445, 514, 760, and 847 nm. Also, the major peak for all species at 514 nm decays by less than 5% over 24 h in ACN (Fig. S6, ESI[†]). All of the radical-cation salts exhibit a faster decay in PC of $\sim 15\%$ over 24 h (Fig. S7, ESI[†]). Due to the low concentration of the active species (0.15 mM) employed in UV-vis measurements, trace impurities in the solvent may

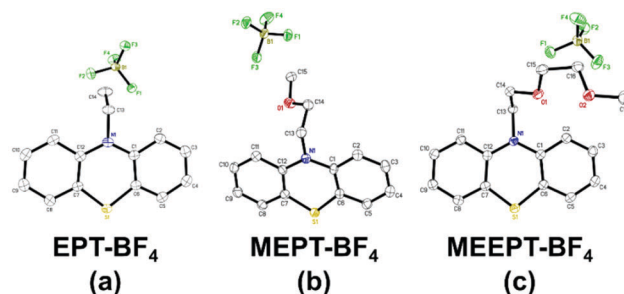


Fig. 4 Thermal ellipsoid plots of the crystal structures of (a) *N*-ethylphenothiazine tetrafluoroborate (EPT- BF_4), (b) *N*-(2-methoxyethyl)phenothiazine tetrafluoroborate (MEPT- BF_4), and (c) *N*-(2-(2-methoxyethoxy)ethyl)phenothiazine tetrafluoroborate (MEEPT- BF_4).

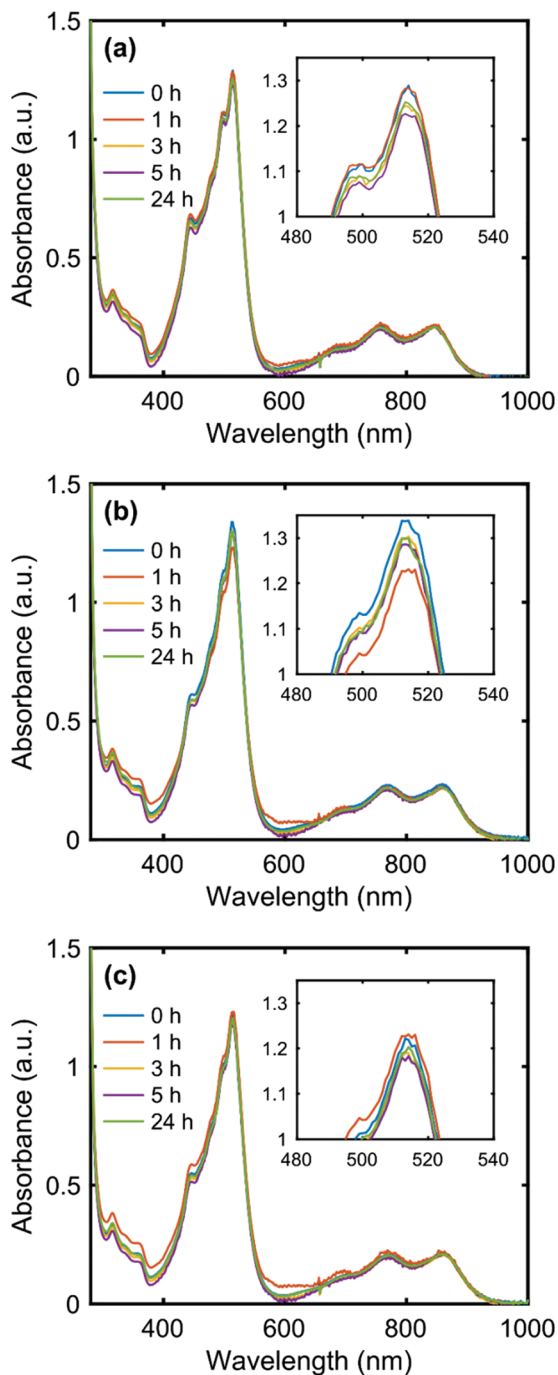


Fig. 5 UV-vis spectra of (a) EPT-BF₄, (b) MEPT-BF₄, and (c) MEEPT-BF₄ at 0.15 mM in ACN, recorded at 0, 1, 3, 5, and 24 h after dissolution. Insets: Expansion of the most intensely absorbing peak in the visible region.

contribute to the observed decay, which may not manifest at higher concentrations. For example, the EPT-BF₄, MEPT-BF₄, and MEEPT-BF₄ radical-cation salts undergo a chemical reaction in the presence of nucleophiles such as water, and the neutral molecules undergo a slow chemical decay in the presence of oxygen. As such, this study moves towards investigating the solubility, stability, and performance of EPT, MEPT, and MEEPT in environments relevant to their implementation in a

flow battery, employing ACN, due to the greater stability of the radical-cations salts in that solvent.

Solubility

Knowledge of the active species solubility is of paramount importance when selecting flow battery operating conditions, because a stable battery can only support an active species concentration as high as the solubility of the least soluble oxidation state. The solubilities of MEPT and MEEPT are significantly higher in organic solvents compared to EPT (*ca.* 0.1 M), perhaps due to the greater polarity of the oligo(glycol) chains relative to the small alkyl group in EPT, as well as the increased disorder arising from the more flexible side-chains (Table 1). MEPT is soluble to > 2 M and MEEPT is miscible with both ACN and our electrolyte of interest, 0.5 M tetraethylammonium tetrafluoroborate (TEABF₄)/ACN. A later flow cell experiment employs this supporting electrolyte composition.

Although MEPT and MEEPT are highly soluble in pure ACN, flow batteries require that the active species remain soluble across all states-of-charge (SOCs) in an electrolyte containing supporting salt, the presence of which can suppress the solubility of redox-active materials.^{31,58,59} As such, we investigated the solubilities (Table 1) of the radical-cation salts (EPT-BF₄, MEPT-BF₄, MEEPT-BF₄) in pure ACN solvent and in 0.5 M TEABF₄/ACN. We found that MEEPT-BF₄ is 3 × to 5 × more soluble than the smaller MEPT-BF₄, and that, unlike the neutral compounds, MEPT-BF₄ solubility does not improve over EPT-BF₄. Additionally, the solubilities of all species decrease in the presence of the supporting salt, agreeing with prior studies.^{31,58,59} The MEEPT/MEEPT-BF₄ couple appears to be the best candidate for flow cell implementation, pending validation of its electrochemical performance, because that couple maintains the highest solubility in both the neutral and oxidized states.

As previously mentioned, economically viable NAQRFBs will require high active-species concentrations (> 1 M).⁹ Several prior studies have investigated redox-active organic molecules that exhibit > 1 M solubility in pure solvent, in the fully discharged state.^{19,20,22–24} All of these studies fail, however, to report active species solubility in an electrolyte, containing supporting salt, or the solubility in the fully charged state. Some studies on metal-centered complexes have considered how dual solutes impact solubility,^{31,58} but still do not mention solubility of the charged species. Arguably, charged species solubilities have been ignored in recent literature due to the difficulty in isolating the charged states of active materials. In the present work, the drastic decreases in MEPT and MEEPT solubilities from the neutral to radical-cation states illustrate

Table 1 Solubilities of the neutral molecules and their radical-cation salts in pure solvent (ACN) and in supporting electrolyte (0.5 M TEABF₄/ACN). Solubilities are reported in molarity (M)

Solvent	EPT, EPT-BF ₄	MEPT, MEPT-BF ₄	MEEPT, MEEPT-BF ₄
ACN	0.25, 0.2	> 2.0, 0.2	Miscible, 0.6
0.5 M TEABF ₄ /ACN	0.1, 0.1	> 2.0, 0.1	Miscible, 0.5

an additional molecular design challenge for redox-active organic molecules. The solubilities of the radical-cation salts thereby limit the maximum feasible operating concentrations for MEPT and MEEPT to 0.1 M and 0.5 M, respectively, in a supporting electrolyte of 0.5 M TEABF₄/ACN. These values are less than required concentrations for economic viability, and addressing the challenge of improving the radical-cation salt solubility is a key step to enabling even higher feasible concentrations for future NAqRFB active materials.

Cyclic voltammetry

CV offers a method of investigating the redox potential, chemical reversibility, kinetics, and diffusion coefficients associated with EPT, MEPT, and MEEPT. Fig. 6 presents cyclic voltammograms of the active species in an electrolyte containing 0.1 M TEABF₄/ACN. Like EPT, the first oxidations of MEPT and MEEPT are chemically reversible in CV experiments, with MEPT and MEEPT exhibiting slightly higher oxidation potentials than EPT (Fig. 6 and Table 2). This trend in oxidation potential is consistent with the increasing adiabatic ionization potentials (IPs, Table 2) from EPT to

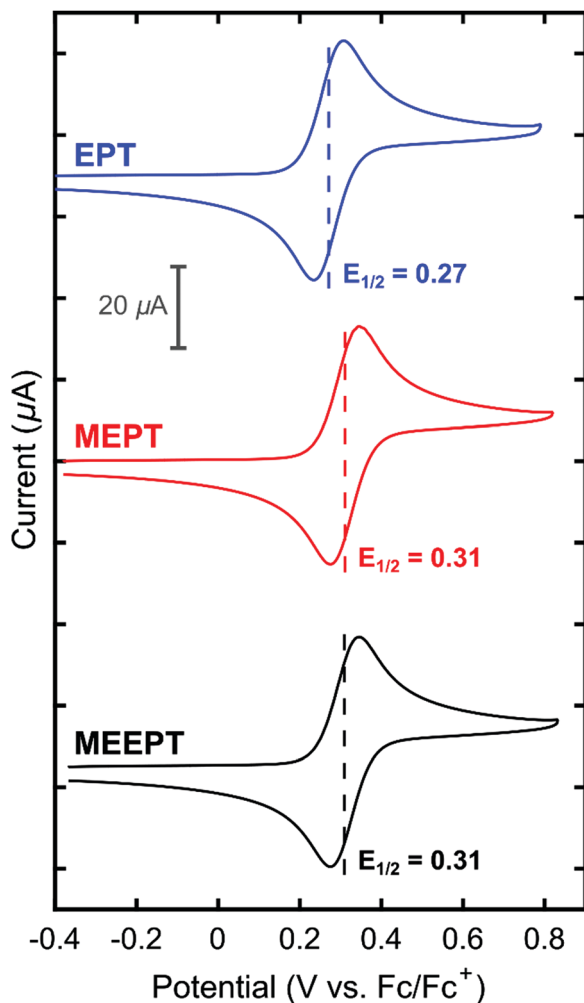


Fig. 6 Cyclic voltammograms (cycle 1) of EPT (blue, top), MEPT (red, middle), and MEEPT (black, bottom) at 1 mM in 0.1 M TEABF₄/ACN. Dashed lines denote the half-wave (redox) potentials ($E_{1/2}$).

Table 2 Calculated adiabatic ionization potentials (IPs), half-wave (redox) potentials ($E_{1/2}$), and diffusion coefficients for EPT, MEPT, and MEEPT. In all cases, TEABF₄ is dissolved at 0.1 M in ACN and the active species concentration was 1 mM

Compound	Adiabatic IP (eV)	$E_{1/2}^{0/+}$ (V vs. Fc/Fc ⁺)	Diffusion coefficient ($\times 10^{-5}$ cm ² s ⁻¹)
EPT	5.08	0.27	1.26
MEPT	5.12	0.31	1.23
MEEPT	5.13	0.31	1.16

MEPT/MEEPT, determined at the B3LYP/6-311G(d,p) level of theory.^{60–63} These calculations were performed with the self-consistent reaction field (SCRF) polarizable continuum method,⁶⁴ implemented in Gaussian09 (revision A.02),⁶⁵ employed to model the acetonitrile ($\epsilon = 35.7$) environment. The variations in IP arise, as expected, from the stronger electron-withdrawing character of the alkylether substituents relative to the ethyl group.

In addition, all three active species display a chemically irreversible second oxidation event at higher potentials (0.8–1.0 V vs. Fc/Fc⁺, Fig. S8, ESI[†]). A scan rate-dependent CV study (Fig. S9, ESI[†]) allows for estimation of diffusion coefficients for each active species (Table 2) using Randles–Sevcik analysis (eqn (1)).⁵⁶ The diffusion coefficients decrease slightly as the size of the active species increases due to increasing solvated radii with increasing molecule size. The CV scan rate study also indicates the electrochemical reversibility of EPT, MEPT, and MEEPT, as the peak separations (~ 60 mV), peak potentials, and peak current ratios (~ 1) are invariant with scan rate.

Bulk electrolysis

Bulk electrolysis experiments allow for further characterization of the electrochemical performance of EPT, MEPT, and MEEPT by assessing the capacity retention of the active species while cycling under dilute conditions for hour time scales. Bulk electrolysis cannot cycle high concentrations of active material due to mass transfer limitations of the stirred electrolyte, and contaminant crossover from the counter electrode can poison the working electrode environment, convoluting capacity-retention data later in the experiment. Nonetheless, bulk electrolysis (Fig. 7) can confirm the ability of the active species to charge and discharge at dilute levels.

All three active species display reasonable capacity retentions of 87.7%, 82.5%, and 96.8% for EPT, MEPT, and MEEPT, respectively. The capacity fades observed in bulk electrolysis likely arise from crossover through the porous glass frit and deleterious interactions with side product species generated in the counter electrode's chamber or on the counter electrode itself. Mean current efficiencies for EPT, MEPT, and MEEPT in bulk electrolysis were 97.6%, 96.1%, and 98.0%, respectively. Losses in current efficiency likely relate to crossover or side reactions amounting to the corresponding capacity fade. The capacity vs. potential cycling curves (Fig. S11, ESI[†]) validate charging and discharging of the anticipated one electron process for each active species at the redox potentials measured *via* CV. Further, the measured charge capacities are extremely close to the theoretical capacities, indicating that all of the

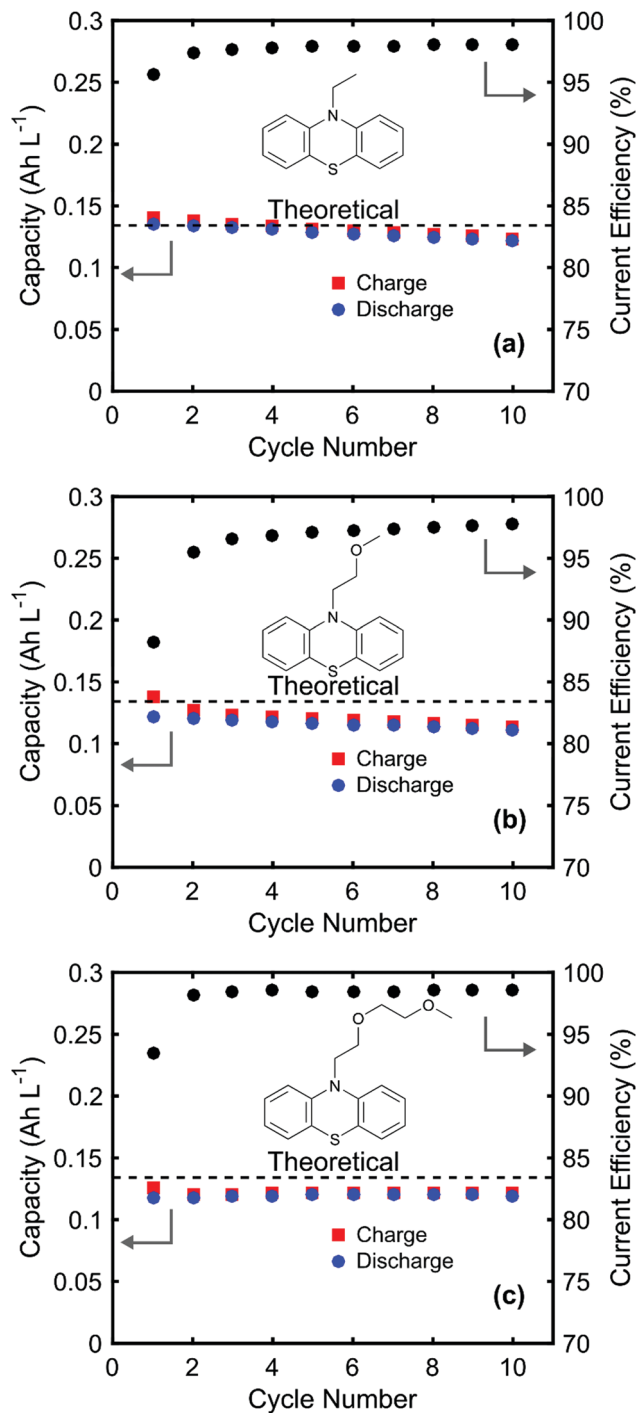


Fig. 7 Capacities and current efficiencies from bulk electrolysis cycling experiments of (a) EPT, (b) MEPT, and (c) MEEPT. Theoretical capacities are 0.134 Ah L^{-1} (0.469 mAh) for each experiment, and 10 cycles completed in 7 h.

active material contributes one electron's worth of storage to the available capacity under dilute conditions. Finally, CVs of the active species collected before and after cycling (Fig. S12 and Table S1, ESI[†]) confirm that the electrochemical behavior of all active species remains the same. Although the CV baseline signals and peak separations change before and after

cycling, these effects are likely due to surface fouling of the glassy-carbon electrode. Table S1 (ESI[†]) shows that the electrochemical behavior intrinsic to the active species (*e.g.*, redox potentials, peak heights, peak height ratios) does not change. This brief bulk electrolysis study indicates that the active species warrant longer duration cycling experiments in a flow cell, where the counter electrode and poor mass transfer do not confound the results.

MEEPT symmetric flow cell cycling

Given that EPT, MEPT, and MEEPT perform very similarly in radical-cation stability, CV, and bulk electrolysis experiments, we use solubility to determine which derivative to use in flow-cell cycling experiments, choosing the most soluble active species, MEEPT. The stability and solubility of the MEEPT-BF₄ radical-cation salt allows for symmetric flow cell cycling, a technique we recently introduced.⁴² The symmetric flow cell technique offers several advantages when investigating the capacity retention of a single active species. First, this technique allows for simultaneous cycling of both the neutral and oxidized species in the MEEPT redox pair to determine MEEPT stability under flow cell conditions in the absence of any other species. Second, unlike bulk electrolysis, symmetric flow cell cycling removes the need for a counter electrode of a dissimilar material, eliminating the possibility of side products crossing from the counter electrode chamber and contaminating the working electrode. Thus, the symmetric flow cell technique offers a more controlled electrolyte environment as compared to bulk electrolysis. Third, the flowing electrolyte improves mass transfer of active species to the electrode surface, enabling higher concentration and high current density studies. Finally, the symmetric flow cell investigates capacity retention using porous carbon electrodes relevant to flow-battery applications (*e.g.*, carbon paper) instead of reticulated vitreous- or glassy-carbon.⁴²

Fig. 8a shows a schematic of the symmetric flow cell, where MEEPT is the starting positive electrolyte (posolyte) active species, and MEEPT-BF₄ is the initial negative electrolyte (negolyte) active species. Accordingly, a tetrafluoroborate anion must migrate across the separator, and the active species on either side of the cell oscillates between MEEPT and MEEPT-BF₄. For all flow cell experiments in this work, both reservoirs initially contain electrolyte pre-mixed at 50% SOC to allow for polarization (Fig. 8b) and impedance measurements (Fig. 8c) prior to cycling. Polarization measurements illustrate the high rate capability of the flow cell employed in this work, achieving current densities as great as $\sim 110 \text{ mA cm}^{-2}$ at $\pm 0.4 \text{ V}$. These high current densities are possible due to a low cell ASR, as indicated by the impedance spectrum in Fig. 8c. The low-frequency intercept denotes the total direct current (DC) contribution (R_{DC}) to the cell impedance ($3.2 \text{ } \Omega \text{ cm}^2$), and closely matches the slope of the polarization curve ($3.3 \text{ } \Omega \text{ cm}^2$) for cell potential magnitudes under 0.15 V , indicating that the Nyquist plot low frequency intercept is a good measure of the cell ASR for small overpotentials.

The ohmic contribution ($R_{\Omega} = 2.3 \text{ } \Omega \text{ cm}^2$) to the cell ASR is similar to that of a prior NAqRFB study employing a Daramic separator and similar supporting electrolyte.³⁰ Further, the

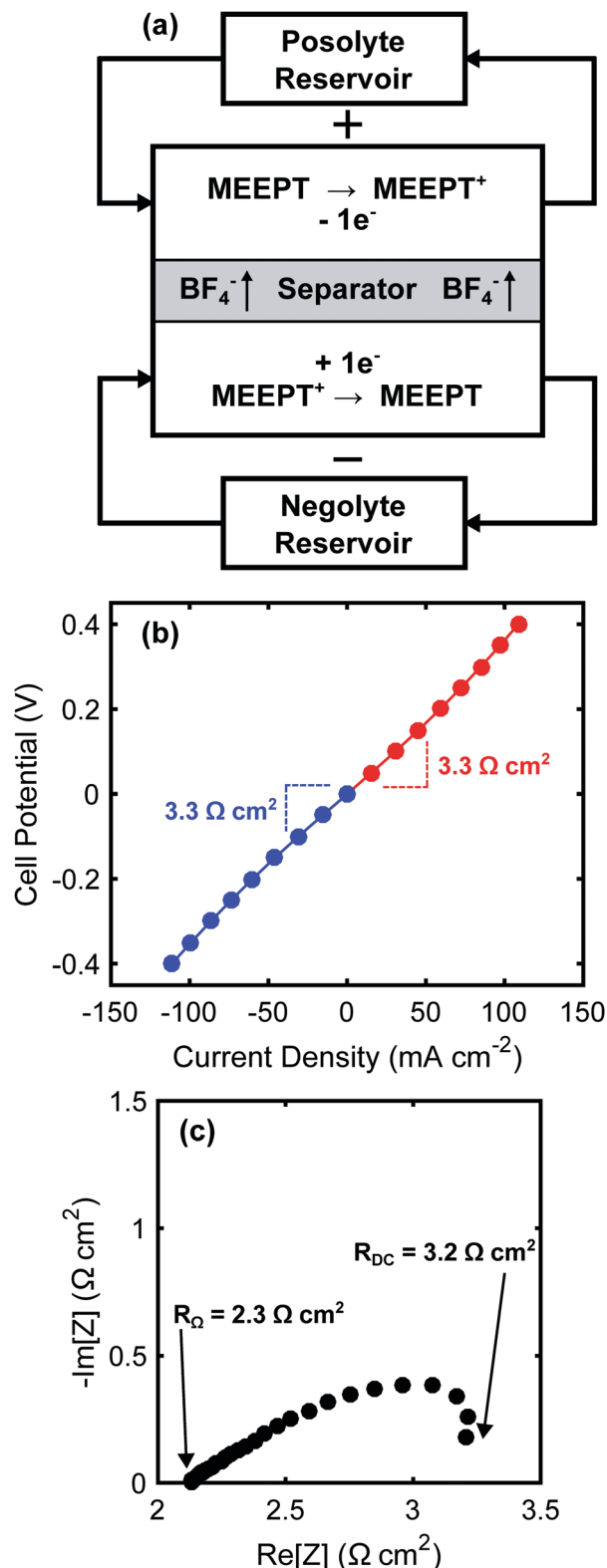


Fig. 8 (a) Schematic of the MEEPT symmetric flow cell during charging. (b) Polarization curve and (c) Nyquist plot of the flow cell at 50% SOC before cycling.

linearity of the polarization curve at low overpotentials (<0.15 V) suggests that the charge transfer (kinetic) resistance contribution

to the total ASR is small and unchanging. Impedance analysis confirms the small charge transfer resistance due to the absence of a distinct charge transfer impedance feature. Redox-active organic molecules in non-aqueous electrolytes typically exhibit fast kinetic rate constants (*i.e.*, greater than $10^{-3} \text{ cm s}^{-1}$),⁹ as confirmed for MEEPT in the CV scan rate study, which leads to negligibly small charge transfer losses.⁴² At higher cell potentials (>0.15 V), the polarization curve begins to deviate from linearity slightly due to the increasing mass-transfer limitation; at even higher overpotentials, the cell would approach limiting current. Overall, the cell ASR in this work is low in comparison to recent NAqRFB cycling literature,^{17,20,66} outperforming the lowest reported ASR to date by a factor of two.³⁰ The ASR reported here is on par with recommended values for enabling cost competitive NAqRFBs ($2.3\text{--}5.0 \Omega \text{ cm}^2$).^{9,10}

The low cell ASR facilitates high rate cycling of MEEPT at high current densities not previously achieved by non-aqueous flow cells. The first flow cell cycling experiment engages a rate study to understand variations in accessed capacity with increasing current density and to select optimized parameters for a long duration cycling experiment. Fig. 9 shows capacity vs. potential curves, as well as the accessed charge and discharge capacities. For constant current cycling at 50, 75, 100, and 125 mA cm^{-2} , the accessed capacities are 97.3%, 86.3%, 66.7%, and 35.0% of the theoretical (13.4 Ah L^{-1}), respectively. As anticipated, the accessed capacity decreases with increasing current density due to larger cell polarization. The rate study also demonstrates the stability of MEEPT and the resiliency of this system's capacity after undergoing high rate cycling; the capacity in cycle 25 rebounded to 99.8% of the accessed capacity in cycle 5.

From the rate study, we chose a current density of 100 mA cm^{-2} to demonstrate long duration cycling of MEEPT. Fig. 10a shows select capacity vs. potential curves over 100 cycles; each curve is nearly identical, indicating that no new electrochemical processes arise during cycling and highlighting again the robust stability of MEEPT. Also, Fig. 10b displays the charge and discharge capacities as a function of cycle number, as well as the current efficiencies. The capacity rises slightly in the first *ca.* 15 cycles because the cell is assembled at 50% SOC, after which the capacity and current efficiencies stabilize. The mean capacity accessed is 76.9% (10.3 Ah L^{-1}) of the theoretical value (13.4 Ah L^{-1}), and after cycle 1, all cycles access were between 74.8 and 77.6% of the theoretical capacity. These charge depths are close to a recommended value of 80% for economically viable cycling of RFBs.⁹ Capacity fade is undetectable over the 100 cycles of the symmetric flow cell experiment, solidifying MEEPT as a highly stable redox-active molecule, especially considering the total runtime (80.6 h) of the experiment. The mean current efficiency for this cell is 99.5%, and given the high capacity retention, current inefficiencies are most likely due to crossover through the porous Daramic separator. After the cycling experiment completed, the flow cell did not show signs of degradation to any of the components, including the Daramic separator, Gore gaskets, carbon paper electrodes, graphite flow fields, tube fittings, tubing, reservoirs, or polypropylene backing plates. As a whole, the long duration flow-cell cycling experiment

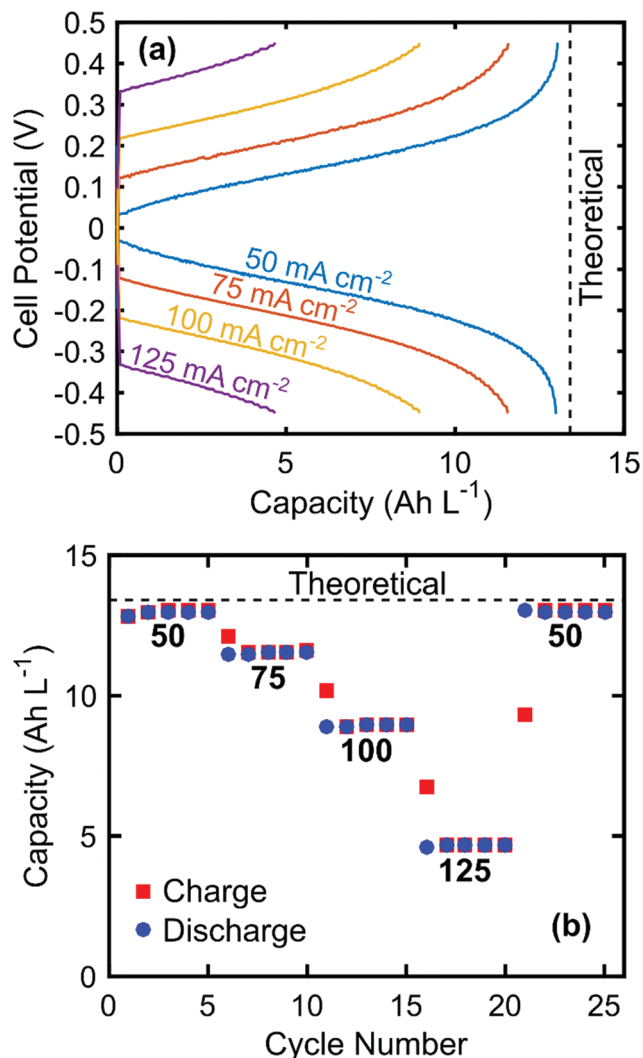


Fig. 9 Rate study of MEEPT cycling in a symmetric flow cell, showing (a) capacity vs. potential for various current densities. Potential curves are from the 5th cycle at each current density. (b) Cycle number vs. capacity for various current densities. Numbers underneath each capacity segment represent current densities with units of mA cm^{-2} . Potential cut-offs imposed during the flow cell experiment were ± 0.45 V. The theoretical capacity (dashed line) is 13.4 Ah L^{-1} (134 mAh), and the experiment runtime was 31.8 h .

combines a robust active material with an advanced cell design, permitting stable, deep charge, and high rate cycling of a NAqRFB active material in an unprecedented manner.

Experimental

General

Phenothiazine (99%), 1-bromo-2-(2-methoxyethoxy)ethane (90%), and sodium hydride (60% dispersion in mineral oil) were purchased from Acros Organics. 2-Chloroethyl methyl ether (98%) and NOBF_4 (98%) were purchased from Alfa Aesar. NOBF_4 was stored and weighed in an argon filled glovebox (MBraun, $\text{O}_2 < 0.1 \text{ ppm}$, $\text{H}_2\text{O} < 0.6 \text{ ppm}$), and removed in a capped vial only immediately prior to use. Other reagents and

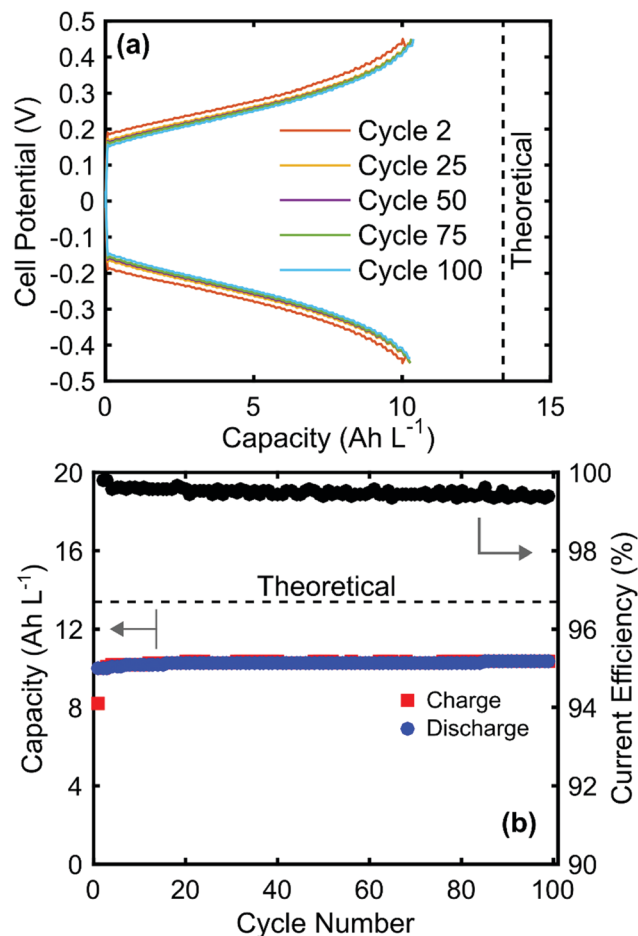


Fig. 10 Constant current cycling of MEEPT in a symmetric flow cell at 100 mA cm^{-2} : (a) capacity vs. potential; (b) charge (red \blacksquare) and discharge capacities (blue \bullet), as well as current efficiencies (black \bullet), as a function of cycle number. Potential cut-offs imposed during the flow cell experiment were ± 0.45 V. The theoretical capacity (dashed line) is 13.4 Ah L^{-1} (134 mAh), and the experiment runtime was 80.6 h .

chromatography solvents were purchased from VWR. Silica gel (65×250 mesh) was purchased from Sorbent Technologies.

All electrochemical measurements were performed in argon-filled gloveboxes ($\text{O}_2 < 0.7 \text{ ppm}$, $\text{H}_2\text{O} < 0.6 \text{ ppm}$) from MBraun or Innovative Technologies. Propylene carbonate (PC, 99.99%) and tetraethylammonium tetrafluoroborate (TEABF_4 , 99.99%) were purchased from BASF and used as received, while anhydrous acetonitrile (ACN) (99.9%) was purchased from Acros Organics. Kryptofix[®] 222 (cryptand, 4,7,13,16,21,24-hexaoxa-1,10-diazabicyclo[8.8.8]-hexacosane, Acros Organics, 98%) and silver tetrafluoroborate (AgBF_4 , Sigma Aldrich, 98%) were used as received. Silver wire was purchased from Alfa Aesar. Silver-silver chloride (Ag/AgCl) reference electrodes were purchased from CH Instruments, removed from their glass housing, and freshly anodized before use. Due to the lack of stable and conductive separators available for use in NAqRFBs, we implemented a Daramic separator to minimize interactions between the separator and active species, as well as eliminate separator decay as a performance degradation mechanism.³¹ In particular, a Daramic

175 separator (thickness = 175 μm , porosity = 58%, mean pore size = 100 nm) was used as received and employed as the separator material in flow cell experiments.

^1H and ^{13}C nuclear magnetic resonance (NMR) spectra were obtained on Varian spectrometers in deuterated chloroform from Cambridge Isotope Laboratories. J values are reported in Hz. Mass spectra were obtained on an Agilent 5973 Network mass selective detector attached to an Agilent 6890N Network GC system. Elemental analyses were performed by Atlantic Microlab Inc. Electron paramagnetic resonance (EPR) spectra were acquired on a Bruker EMXplus spectrometer with a PremiumX bridge containing an ER 4119HS-W1 high sensitivity cavity. To prepare the sample, 5 mg of EPT-BF₄, MEPT-BF₄, or MEEPT-BF₄ was dissolved in 20 mL of DCM and transferred to a 4 mm Wilmad-Labglass quartz EPR tube. The spectrum was acquired immediately thereafter at room temperature.

Synthesis of neutral compounds

N-Ethylphenothiazine (EPT) was synthesized according to a prior report.⁴⁸ For small-scale synthesis of MEPT and MEEPT, phenothiazine (1.99 g, 10.0 mmol) was dissolved in anhydrous *N,N*-dimethylformamide (DMF, 20 mL) under nitrogen atmosphere. A 60% dispersion of sodium hydride (NaH) in mineral oil (0.48 g, 12 mmol) was added, and the reaction mixture was heated to 60 °C for 30 min. Then, 2-chloroethyl methyl ether (1.10 mL, 12 mmol, for MEPT) or 1-bromo-2-(2-methoxyethoxy)ethane (1.62 mL, 12 mmol, for MEEPT) was added, and the reaction mixture was stirred at 60 °C for 12 h. The reaction was quenched by pouring the contents into ice water, after which the organic components were extracted with ethyl acetate three times, and the combined extracts were washed with brine. The organic extracts were dried over magnesium sulfate (MgSO₄), filtered to remove solids, and concentrated by rotary evaporation. The crude product was purified by column chromatography using a gradient of 0 to 10% ethyl acetate in hexanes to afford the desired products after concentration by rotary evaporation.

***N*-(2-Methoxyethyl)phenothiazine (MEPT).** Yield: 2.16 g (84%). White crystalline solid (m.p. 47 °C). ^1H NMR (400 MHz, CDCl₃) δ 1.57 (H₂O), 3.40 (s, 3H), 3.76 (t, 2H, J = 6.4 Hz), 4.09 (t, 2H, J = 6.4 Hz), 6.89–6.94 (m, 4H), 7.12–7.17 (m, 4H). ^{13}C NMR (100 MHz, CDCl₃) δ 47.5, 59.2, 69.9, 115.3, 122.7, 124.8, 127.5, 127.6, 145.1. EI-MS: m/z 257 (54%), 212 (100%), 198 (20%), 180 (61%). Anal. calcd for C₁₅H₁₅NOS C, 70.01; H, 5.88; N, 5.44. Found C, 69.99; H, 5.91; N, 5.39.

***N*-(2-(2-Methoxyethoxy)ethyl)phenothiazine (MEEPT).** Yield: 2.22 g (74%). pale yellow oil. ^1H NMR (400 MHz, CDCl₃, Me₄Si) δ 1.55 (H₂O), 3.38 (s, 3H), 3.53–3.56 (m, 2H), 3.64–3.66 (m, 2H), 3.85 (t, 2H, J = 6.5 Hz), 4.12 (t, 2H, J = 6.5 Hz), 6.90–6.93 (m, 4H), 7.11–7.16 (m, 4H). ^{13}C NMR (100 MHz, CDCl₃, Me₄Si) δ 47.5, 59.2, 68.5, 70.8, 72.1, 115.4, 122.8, 124.8, 127.5, 127.6, 145.1. EI-MS: m/z 301 (48%), 212 (100%), 198 (22%), 180 (46%). Anal. calcd for C₁₇H₁₉NO₂S C, 67.75; H, 6.35; N, 4.65. Found C, 67.48; H, 6.41; N, 4.88.

For a large-scale synthesis of MEEPT, phenothiazine (10.00 g, 50.25 mmol) was dissolved in anhydrous DMF (120 mL) under nitrogen atmosphere in an oven-dried, three-neck round-bottomed

flask equipped with a reflux condenser. A 60% dispersion of NaH in mineral oil (2.90 g, 72.5 mmol) was added, and the reaction mixture was stirred for 15 min. Then, 1-bromo-2-(2-methoxyethoxy)ethane (8.10 mL, 60.2 mmol) was added, and the reaction mixture was heated and stirred at 60 °C for 16 h. The reaction was quenched by pouring the reaction mixture into ice water, after which the organic components were extracted with diethyl ether, and the organic layer was washed with brine. The organic extracts were dried over MgSO₄, filtered to remove solids, and concentrated by rotary evaporation. The crude product was purified by column chromatography using a gradient of 0 to 10% ethyl acetate in hexanes to afford the desired products after concentration by rotary evaporation. Yield: 13.40 g (88%). ^1H NMR and mass spectra matched those observed for the small-scale syntheses.

Synthesis of radical-cation salts

General procedure. The neutral compound (1 mmol) and anhydrous DCM (10 mL) were added to an oven-dried, round-bottomed flask cooled under nitrogen atmosphere. The resulting solution was purged with nitrogen for 20 min. NOBF₄ (0.122 g, 1.05 mmol) was added to the solution, which immediately turned dark orange. The reaction vessel was capped with a rubber septum and the reaction mixture was stirred under nitrogen for 1 h, after which diethyl ether (20 mL) was added gradually with continued stirring, producing a dark precipitate. The precipitate was filtered, then dissolved in DCM (10 mL) and re-precipitated with a second addition of diethyl ether (20 mL). This process was repeated once more to ensure removal of any unreacted starting material. The final precipitate was dried under vacuum and stored in an argon filled glovebox.

***N*-(2-Ethylphenothiazine tetrafluoroborate salt (EPT-BF₄)).** EPT (5.04 g, 22.2 mmol) and NOBF₄ (2.54 g, 23.3 mmol) were reacted according to the general procedure to yield EPT-BF₄ (4.53 g, 65%). Crystals for X-ray diffraction (XRD) were grown in DCM and toluene. A saturated solution of salt in DCM was placed in a NMR tube. Toluene was run down the side of the tube using a syringe to form a discrete layer. The NMR tube was capped and placed in the freezer, and crystals formed at the interface of the solvent layers.

***N*-(2-Methoxyethyl)phenothiazine tetrafluoroborate salt (MEPT-BF₄)).** MEPT (3.00 g, 11.6 mmol) and NOBF₄ (1.43 g, 12.2 mmol) were reacted according to the general procedure to yield MEPT-BF₄ (2.51 g, 61%). Crystals for XRD were grown by dissolving the salt in DCM and placing this vial inside of another vial containing pentane. The outer vial was capped and was placed in a freezer, and crystals formed through vapor diffusion.

***N*-(2-(2-Methoxyethoxy)ethyl)phenothiazine tetrafluoroborate salt (MEEPT-BF₄)).** MEEPT (16.1 g, 53.4 mmol) and NOBF₄ (6.55 g, 56.1 mmol) were reacted according to the general procedure to yield MEEPT-BF₄ (12.5 g, 60%). Crystals for XRD were grown in DCM and toluene. A saturated solution of salt in DCM was placed in a NMR tube. Toluene was run down the side of the tube using a syringe to form a discrete layer. The NMR tube was capped and placed in a freezer, and crystals formed at the interface of the solvent layers.

Radical cation stability studies

An Agilent diode-array spectrometer was used to collect UV-vis absorption spectra using ACN or PC as the solvent. Radical-cation salts were dissolved at 0.15 mM in the appropriate solvent and pipetted into optical glass cuvettes (Starna) with a 1 cm path length. Solutions were added to the cuvettes inside an argon filled glovebox and then sealed with a Teflon screw cap. The sealed cuvette was then removed from the glovebox for spectral analysis. Spectra were collected at 0, 1, 3, 5, and 24 h after dissolution.

Solubility

The solubility limits of the neutral molecules (EPT, MEPT, and MEEPT) and the radical-cation salts (EPT-BF₄, MEPT-BF₄, and MEEPT-BF₄) in pure ACN and an electrolyte comprised of ~0.5 M TEABF₄/ACN were estimated by a shake-flask method. Active material was added in excess to either pure ACN or the electrolyte. Then, the solution was diluted slowly, stirring between additions, with either pure ACN or the electrolyte. The dilution process continued until the active species was dissolved, as determined by visual inspection.

Cyclic voltammetry

CV experiments were performed using a custom three-electrode cell comprised of a 3 mm diameter glassy-carbon working electrode (CH Instruments), platinum wire counter electrode (CH Instruments), and freshly anodized, un-fritted Ag/AgCl wire reference electrode. Electrochemical data was collected on a CH Instruments 650E potentiostat. No solution resistance compensation (*iR* correction) was applied. Electrolytes were comprised of 1 mM neutral active material (EPT, MEPT, or MEEPT), 0.1 M TEABF₄, and either ACN or PC as the solvent. In some experiments, ~0.7 mM ferrocene was added as an internal reference. Redox (half-wave) potentials ($E_{1/2}$) were calculated as the mean potential between CV peaks from voltammograms recorded at 100 mV s⁻¹ and are reported relative to the Fc/Fc⁺ internal reference (Fig. S8, ESI[†]). Diffusion coefficients of the active species were determined using Randles-Sevcik analysis (eqn (1)) and the peak currents of voltammograms, without the ferrocene internal reference, at the following scan rates: 25, 50, 75, 100, 200, 300, 400, and 500 mV s⁻¹ (Fig. S9, ESI[†]). In eqn (1), i_p is the peak current (A), n is the number of electrons transferred (mol_e mol⁻¹), A is the electrode surface area (cm²), C is the reactant concentration (mol cm⁻³), s is the scan rate (V s⁻¹), R is the gas constant (J mol⁻¹ K⁻¹), T is temperature (K), and D is the diffusion coefficient (cm² s⁻¹).⁵⁶

$$i_p = 0.4463nFAC \left(\frac{nFsD}{RT} \right)^{\frac{1}{2}} \quad (1)$$

Bulk electrolysis

Bulk electrolysis experiments were performed in custom H-cells (Fig. S10, ESI[†]), similar to those reported by Laramie *et al.*,³¹ which have two 3.5 mL electrolyte chambers separated by an ultra-fine porous glass frit (P5, Adams and Chittenden).

The glass frit helped to minimize species crossover between the two compartments. In one chamber, a piece of reticulated vitreous carbon (45 PPI, Duocell) served as the working electrode, and a fritted Ag/Ag(cryptand)⁺ reference electrode⁵⁷ contained saturated cryptand, 10 mM AgBF₄, and 0.5 M TEABF₄ in PC. In the second chamber, another piece of reticulated vitreous carbon served as the counter electrode. Both the working and counter electrode chambers were continuously stirred during bulk electrolysis cycling. A Biologic VMP3 potentiostat applied a constant current of 0.469 mA, equivalent to a C-rate of 1C, for 10 cycles (7 h). Potential cut-offs of ~0.1 and 0.5 V vs. Fc/Fc⁺ were imposed on the working electrode to avoid accessing undesired redox couples or electrolyte decomposition. A 3 mm glassy-carbon working electrode (CH Instruments) was used to record CVs of the electrolyte in the working electrode chamber before and after cycling. Electrolytes comprised of 5 mM neutral active species (EPT, MEPT, or MEEPT), 1 M TEABF₄, and ACN were added to the working electrode chamber, while the counter-electrode chamber contained electrolytes of 5 mM radical-cation active species (EPT-BF₄, MEPT-BF₄, or MEEPT-BF₄), 1 M TEABF₄, and ACN.

Symmetric flow cell cycling

Small volume custom flow cells with interdigitated flow fields, as previously described by Milshtein *et al.*, were used in this work (Fig. 2).⁴² Flow cell backing plates were machined from polypropylene, which was selected due to its chemical compatibility with ACN. Flow fields were machined from 3.18 mm thick impregnated graphite (G347B, MWI, Inc.). Electrodes were cut from 190 ± 30 μm thick carbon paper (25 AA, SGL group) and used as received without any pre-treatments. Two pieces of carbon paper were layered together to serve as electrodes for both sides of the flow cell and were compressed by ~20%. A single layer of Daramic 175 served as the battery separator material. The electrodes and separator were sealed into the cell using gaskets cut from flexible polytetrafluoroethylene gasket tape (Gore). The assembled cells had geometric active areas of 2.55 cm². Flow cells were assembled outside of the glovebox and then dried for at least 1 h under vacuum (-91 kPa_g) before beginning electrochemical testing. All flow cell cycling, impedance, and polarization measurements were performed inside an argon filled glovebox.

Sealed jars (10 mL, Savillex), made from perfluoroalkoxy alkane (PFA), housed the electrolyte. A peristaltic pump (Masterflex L/S Series) carried the electrolyte into the flow cell at 10 mL min⁻¹. Norprene tubing (Masterflex) was used inside the pump head, while PFA tubing (Swagelok) connected the pump head, reservoir, and flow cell together. All tubing had an inner diameter of 1.6 mm. All tubing connections were coupled together with PFA or stainless steel compression fittings (Swagelok). The fully assembled and filled cell is shown in Fig. S13 (ESI[†]).

Starting electrolytes for flow cell experiments were comprised of 0.25 M MEEPT/0.25 M MEEPT-BF₄/0.5 M TEABF₄/ACN, so that the battery was at 50% SOC. This initial configuration allowed impedance and polarization measurements to be collected at 50% SOC prior to beginning cycling experiments. Each reservoir

contained 0.5 M total active species in 10 mL of electrolyte, enabling a theoretical capacity of 13.4 Ah L^{-1} (134 mAh). Impedance measurements were recorded about the cell open-circuit voltage (OCV) at 50% SOC, with an amplitude of 10 mV, over a frequency range of 200 kHz to 5 mHz. Polarization measurements were collected by initiating potentiostatic holds for 1 min in alternating ± 50 mV steps, allowing for data collection over the range of -0.4 to 0.4 V without significantly changing electrolyte SOC. Data points were recorded every 0.1 s, and the mean current and potential values of the final 50% of data points were used in the I - V curves.

Before beginning symmetric flow cell cycling experiments, a constant current pre-discharge was performed to bring the cell to its fully charged state. Then, cycling experiments were performed by applying a constant current density, calculated from the geometric electrode area (2.55 cm^2). Two total flow cell experiments were performed. In the first experiment, the current density was varied from 50 to 125 mA cm^{-2} , in increments of 25 mA cm^{-2} , for 5 cycles at each current density, and potential cut-offs of ± 0.45 V were imposed. The cell was then returned to the initial current density of 50 mA cm^{-2} for 5 additional cycles. This rate study was completed in 31.8 h. In the second experiment, the flow cell underwent constant current cycling for 100 cycles (80.6 h) at a current density of 100 mA cm^{-2} , with potential cut-offs of ± 0.45 V.

Conclusions

In this work, we demonstrated stable, soluble redox-active organic molecules and a low ASR flow cell for NAqRFBs. By molecular modification of a stable but low solubility parent molecule (EPT), we synthesized two new molecules, MEPT and MEEPT, in a single step each. The inexpensive phenothiazine precursor and straightforward synthesis may enable low-cost scale-up of the new derivatives, which are miscible in ACN and an electrolyte comprised of 0.5 M TEABF₄/ACN. Although both the neutral MEPT and MEEPT exhibit high solubilities, the MEEPT-BF₄ radical-cation salt exhibited superior solubility over MEPT-BF₄. The solubility of both radical-cation salts needs to be improved for practical application, presenting a new challenge for rational molecular design. A decay study of the EPT-BF₄, MEPT-BF₄, and MEEPT-BF₄ radical-cation salts under dilute conditions indicates that all three radical species exhibit essentially identical stability. CV shows that all of the molecules considered exhibit electrochemically reversible behavior. The functionalized derivatives (MEPT and MEEPT) have a redox potential of 0.31 V vs. Fc/Fc⁺, a value slightly higher than that of EPT and in agreement with the calculated IPs. Bulk electrolysis illustrates that all three active species cycle similarly under dilute conditions. Further, we designed a high performance flow cell, with IDFFs and thin carbon paper electrodes, that demonstrates the lowest ASR for a NAqRFB to date (3.2 – $3.3 \Omega \text{ cm}^2$), permitting current densities $> 100 \text{ mA cm}^{-2}$. Combining the most soluble compound investigated, MEEPT, with the high performance flow cell, we first engaged a rate study, illustrating

the durability of MEEPT and the flow cell's achievable high current densities. Finally, extended cycling of MEEPT at a constant current density of 100 mA cm^{-2} , with undetectable capacity fade after 100 cycles of deep charging, highlights the unprecedented performance realized through the combination of a robust active material and high performance flow cell.

The molecular and cell engineering principles outlined in this work can be extended to other electrolyte systems proposed for NAqRFBs. Molecular modification of EPT represents a logical pathway towards stable and soluble molecules *via* facile synthesis, and towards low-cost NAqRFBs with long cycle lifetimes, inexpensive electrolytes, and small mass-transfer losses. The flow cell implements prior advances in aqueous RFB architecture to improve the ohmic and mass-transfer resistances over other non-aqueous flow cell designs. Future molecular engineering will aim to enhance the solubility of the radical-cation species by introducing asymmetry to the active species and varying the counter-anion type.⁶⁷ Future cell engineering will focus on scale-up and further ASR reduction by minimizing separator thickness, increasing operating concentration, and lowering contact resistances.

Acknowledgements

Molecular synthesis and characterization studies were supported by the National Science Foundation (NSF), Division of Chemistry under Award Number CHE-1300653 and through the Experimental Program to Stimulate Competitive Research (EPSCoR) Award Number 1355438. Bulk electrolysis and flow cell studies were supported as part of the Joint Center for Energy Storage Research (JCESR), an Energy Innovation Hub funded by the U.S. Department of Energy, Office of Science, Basic Energy Sciences. SAO and CR thank the University of Kentucky for start-up funds. JDM acknowledges additional financial support from the NSF Graduate Research Fellowship Program (DGE 1256260). The authors thank Daramic for providing samples of battery separators.

Notes and references

- 1 I. Gyuk, M. Johnson, J. Vetrano, K. Lynn, W. Parks, R. Handa, L. Kannberg, S. Hearne, K. Waldrip and R. Braccio, *Grid Energy Storage*, US Department of Energy, Washington DC, 2013.
- 2 P. Denholm, E. Ela, B. Kirby and M. Milligan, *The Role of Energy Storage with Renewable Electricity Generation*. NREL/TP-6A2-47187, 2010.
- 3 A. Z. Weber, M. M. Mench, J. P. Meyers, P. N. Ross, J. T. Gostick and Q. Liu, *J. Appl. Electrochem.*, 2011, **41**, 1137–1164.
- 4 P. Leung, X. Li, C. Ponce de León, L. Berlouis, C. T. J. Low and F. C. Walsh, *RSC Adv.*, 2012, **2**, 10125.
- 5 A. Parasuraman, T. M. Lim, C. Menictas and M. Skyllas-Kazacos, *Electrochim. Acta*, 2013, **101**, 27–40.
- 6 S.-H. Shin, S.-H. Yun and S.-H. Moon, *RSC Adv.*, 2013, **3**, 9095.

- 7 W. Wang, Q. Luo, B. Li, X. Wei, L. Li and Z. Yang, *Adv. Funct. Mater.*, 2013, **23**, 970–986.
- 8 P. Alotto, M. Guarnieri and F. Moro, *Renewable Sustainable Energy Rev.*, 2014, **29**, 325–335.
- 9 R. M. Darling, K. G. Gallagher, J. A. Kowalski, S. Ha and F. R. Brushett, *Energy Environ. Sci.*, 2014, **7**, 3459–3477.
- 10 R. Darling, K. Gallagher, W. Xie, L. Su and F. Brushett, *J. Electrochem. Soc.*, 2016, **163**, A5029–A5040.
- 11 *Nonaqueous Electrochemistry*, ed. D. Aurbach, Marcel Dekker, New York, 1999.
- 12 W. Wang and V. Sprenkle, *Nat. Chem.*, 2016, **8**, 204–206.
- 13 M. L. Perry and A. Z. Weber, *J. Electrochem. Soc.*, 2016, **163**, A5064–A5067.
- 14 Z. Li, S. Li, S. Liu, K. Huang, D. Fang, F. Wang and S. Peng, *Electrochem. Solid-State Lett.*, 2011, **14**, A171–A173.
- 15 S.-K. Park, J. Shim, J. Yang, K.-H. Shin, C.-S. Jin, B. S. Lee, Y.-S. Lee and J.-D. Jeon, *Electrochem. Commun.*, 2015, **59**, 68–71.
- 16 F. R. Brushett, J. T. Vaughney and A. N. Jansen, *Adv. Energy Mater.*, 2012, **2**, 1390–1396.
- 17 X. Wei, W. Xu, J. Huang, L. Zhang, E. Walter, C. Lawrence, M. Vijayakumar, W. A. Henderson, T. Liu, L. Cosimbescu, B. Li, V. Sprenkle and W. Wang, *Angew. Chem., Int. Ed.*, 2015, **54**, 8684–8687.
- 18 A. P. Kaur, N. E. Holubowitch, S. Ergun, C. F. Elliott and S. A. Odom, *Energy Technol.*, 2015, **3**, 476–480.
- 19 C. S. Sevov, R. E. M. Brouner, E. Chénard, R. S. Assary, J. S. Moore, J. Rodríguez-López and M. S. Sanford, *J. Am. Chem. Soc.*, 2015, **137**, 14465–14472.
- 20 W. Duan, R. S. Vemuri, J. D. Milshtein, S. Laramie, R. D. Dmello, J. Huang, L. Zhang, D. Hu, V. Murugesan, W. Wang, J. Liu, R. Darling, L. Thompson, K. C. Smith, J. Moore, F. R. Brushett and X. Wei, *J. Mater. Chem. A*, 2016, **4**, 5448–5456.
- 21 R. A. Potash, J. R. McKone, S. Conte and H. D. Abruna, *J. Electrochem. Soc.*, 2016, **163**, A338–A344.
- 22 X. Wei, W. Xu, M. Vijayakumar, L. Cosimbescu, T. Liu, V. Sprenkle and W. Wang, *Adv. Mater.*, 2014, **26**, 7649–7653.
- 23 J. Huang, L. Su, J. A. Kowalski, J. L. Barton, M. Ferrandon, A. K. Burrell, F. R. Brushett and L. Zhang, *J. Mater. Chem. A*, 2015, **3**, 14971–14976.
- 24 J. Huang, L. Cheng, R. S. Assary, P. Wang, Z. Xue, A. K. Burrell, L. A. Curtiss and L. Zhang, *Adv. Energy Mater.*, 2015, **5**, 1401782.
- 25 K. Takechi, Y. Kato and Y. Hase, *Adv. Mater.*, 2015, 2501–2506.
- 26 Y. Matsuda, K. Tanaka, M. Okada, Y. Takasu, M. Morita and T. Matsumura-Inoue, *J. Appl. Electrochem.*, 1988, **18**, 909–914.
- 27 M. H. Chakrabarti, E. P. Lindfield Roberts and M. Saleem, *Int. J. Green Energy*, 2010, **7**, 445–460.
- 28 M. H. Chakrabarti, E. P. L. Roberts, C. Bae and M. Saleem, *Energy Convers. Manage.*, 2011, **52**, 2501–2508.
- 29 M. H. Chakrabarti, R. A. W. Dryfe and E. P. L. Roberts, *Electrochim. Acta*, 2007, **52**, 2189–2195.
- 30 I. L. Escalante-García, J. S. Wainright, L. T. Thompson and R. F. Savinell, *J. Electrochem. Soc.*, 2015, **162**, A363–A372.
- 31 S. M. Laramie, J. D. Milshtein, T. M. Breault, F. R. Brushett and L. T. Thompson, *J. Power Sources*, 2016, **327**, 681–692.
- 32 P. J. Cabrera, X. Yang, J. A. Suttill, K. L. Hawthorne, R. E. M. Brouner, M. S. Sanford and L. T. Thompson, *J. Phys. Chem. C*, 2015, **119**, 15882–15889.
- 33 P. J. Cabrera, X. Yang, J. A. Suttill, R. E. M. Brouner, L. T. Thompson and M. S. Sanford, *Inorg. Chem.*, 2015, **54**, 10214–10223.
- 34 N. S. Hudak, L. J. Small, H. D. Pratt and T. M. Anderson, *J. Electrochem. Soc.*, 2015, **162**, A2188–A2194.
- 35 M.-S. Park, N.-J. Lee, S.-W. Lee, K. J. Kim, D.-J. Oh and Y.-J. Kim, *ACS Appl. Mater. Interfaces*, 2014, **6**, 10729–10735.
- 36 J. Mun, M.-J. Lee, J.-W. Park, D.-J. Oh, D.-Y. Lee and S.-G. Doo, *Electrochem. Solid-State Lett.*, 2012, **15**, A80–A82.
- 37 P. J. Cappillino, H. D. Pratt, N. S. Hudak, N. C. Tomson, T. M. Anderson and M. R. Anstey, *Adv. Energy Mater.*, 2014, **4**, 1300566.
- 38 X. Wei, L. Cosimbescu, W. Xu, J. Z. Hu, M. Vijayakumar, J. Feng, M. Y. Hu, X. Deng, J. Xiao, J. Liu, V. Sprenkle and W. Wang, *Adv. Energy Mater.*, 2015, **5**, 1400678.
- 39 G. Nagarjuna, J. Hui, K. J. Cheng, T. Lichtenstein, M. Shen, J. S. Moore and J. Rodríguez-López, *J. Am. Chem. Soc.*, 2014, **136**, 16309–16316.
- 40 J. Winsberg, T. Hagemann, S. Muench, C. Friebe, B. Häupler, T. Janoschka, S. Morgenstern, M. D. Hager and U. S. Schubert, *Chem. Mater.*, 2016, **28**, 3401–3405.
- 41 S. H. Oh, C.-W. Lee, D. H. Chun, J.-D. Jeon, J. Shim, K. H. Shin and J. H. Yang, *J. Mater. Chem. A*, 2014, **2**, 19994–19998.
- 42 J. D. Milshtein, J. L. Barton, R. M. Darling and F. R. Brushett, *J. Power Sources*, 2016, **327**, 151–159.
- 43 W. Wang, W. Xu, L. Cosimbescu, D. Choi, L. Li and Z. Yang, *Chem. Commun.*, 2012, **48**, 6669–6671.
- 44 S. Ergun, C. F. Elliott, A. P. Kaur, S. R. Parkin and S. A. Odom, *Chem. Commun.*, 2014, **50**, 5339–5341.
- 45 S. Ergun, C. F. Elliott, A. P. Kaur, S. R. Parkin and S. A. Odom, *J. Phys. Chem. C*, 2014, **118**, 14824–14832.
- 46 K. A. Narayana, M. D. Casselman, C. F. Elliott, S. Ergun, S. R. Parkin, C. Risko and S. A. Odom, *ChemPhysChem*, 2015, **16**, 1179–1189.
- 47 A. P. Kaur, S. Ergun, C. F. Elliott and S. A. Odom, *J. Mater. Chem. A*, 2014, **2**, 18190–18193.
- 48 S. A. Odom, S. Ergun, P. P. Poudel and S. R. Parkin, *Energy Environ. Sci.*, 2014, **7**, 760–767.
- 49 D. S. Aaron, Q. Liu, Z. Tang, G. M. Grim, A. B. Papandrew, A. Turhan, T. A. Zawodzinski and M. M. Mench, *J. Power Sources*, 2012, **206**, 450–453.
- 50 Q. H. Liu, G. M. Grim, A. B. Papandrew, A. Turhan, T. A. Zawodzinski and M. M. Mench, *J. Electrochem. Soc.*, 2012, **159**, A1246–A1252.
- 51 B. Huskinson, M. P. Marshak, C. Suh, S. Er, M. R. Gerhardt, C. J. Galvin, X. Chen, A. Aspuru-Guzik, R. G. Gordon and M. J. Aziz, *Nature*, 2014, **505**, 195–198.
- 52 Q. Chen, M. R. Gerhardt, L. Hartle and M. J. Aziz, *J. Electrochem. Soc.*, 2016, **163**, A5010–A5013.
- 53 Q. Chen, L. Eisenach and M. J. Aziz, *J. Electrochem. Soc.*, 2016, **163**, A5057–A5063.
- 54 R. M. Darling and M. L. Perry, *J. Electrochem. Soc.*, 2014, **161**, A1381–A1387.

- 55 C. R. Dennison, E. Agar, B. Akuzum and E. C. Kumbur, *J. Electrochem. Soc.*, 2016, **163**, A5163–A5169.
- 56 R. G. Compton and C. E. Banks, *Understanding Voltammetry*, Imperial College Press, London, 2nd edn, 2011.
- 57 A. Lewandowski, M. Osińska, A. Swiderska-Mocek and M. Galinski, *Electroanalysis*, 2008, **20**, 1903–1908.
- 58 A. A. Shinkle, T. J. Pomaville, A. E. S. Sleightholme, L. T. Thompson and C. W. Monroe, *J. Power Sources*, 2014, **248**, 1299–1305.
- 59 J. R. Dahn, J. Jiang, L. M. Moshurchak, M. D. Fleischauer, C. Buhrmester and L. J. Krause, *J. Electrochem. Soc.*, 2005, **152**, A1283–A1289.
- 60 C. Lee, W. Yang and R. G. Parr, *Phys. Rev. B: Condens. Matter Mater. Phys.*, 1988, **37**, 785.
- 61 A. D. Becke, *Phys. Rev. A: At., Mol., Opt. Phys.*, 1988, **38**, 3098–3100.
- 62 A. D. Becke, *J. Chem. Phys.*, 1993, **98**, 5648.
- 63 R. Krishnan, J. S. Binkley, R. Seeger and J. A. Pople, *J. Chem. Phys.*, 1980, **72**, 650.
- 64 J. Tomasi, B. Mennucci and R. Cammi, *Chem. Rev.*, 2005, **105**, 2999–3094.
- 65 M. J. Frisch, G. W. Trucks, H. B. Schlegel, G. E. Scuseria, M. A. Robb, J. R. Cheeseman, G. Scalmani, V. Barone, B. Mennucci, G. A. Petersson, H. Nakatsuji, M. Caricato, X. Li, H. P. Hratchian, A. F. Izmaylov, J. Bloino, G. Zheng, J. L. Sonnenberg, M. Hada, M. Ehara, K. Toyota, R. Fukuda, J. Hasegawa, M. Ishida, T. Nakajima, Y. Honda, O. Kitao, H. Nakai, T. Vreven, J. A. Montgomery Jr., J. E. Peralta, F. Ogliaro, M. Bearpark, J. J. Heyd, E. Brothers, K. N. Kudin, V. N. Staroverov, R. Kobayashi, J. Normand, K. Raghavachari, A. Rendell, J. C. Burant, S. S. Iyengar, J. Tomasi, M. Cossi, N. Rega, J. M. Millam, M. Klene, J. E. Knox, J. B. Cross, V. Bakken, C. Adamo, J. Jaramillo, R. Gomperts, R. E. Stratmann, O. Yazyev, A. J. Austin, R. Cammi, C. Pomelli, J. W. Ochterski, R. L. Martin, K. Morokuma, V. G. Zakrzewski, G. A. Voth, P. Salvador, J. J. Dannenberg, S. Dapprich, A. D. Daniels, O. Farkas, J. B. Foresman, J. V. Ortiz, J. Cioslowski and D. J. Fox, Gaussian, Inc., Wallingford CT, 2009.
- 66 J.-H. Kim, K. J. Kim, M.-S. Park, N. J. Lee, U. Hwang, H. Kim and Y.-J. Kim, *Electrochem. Commun.*, 2011, **13**, 997–1000.
- 67 L. Cosimbescu, X. Wei, M. Vijayakumar, W. Xu, M. L. Helm, S. D. Burton, C. M. Sorensen, J. Liu, V. Sprenkle and W. Wang, *Sci. Rep.*, 2015, **5**, 14117.